



## Study on relieving residual stress of friction stir welded joint of 2219 aluminum alloy using cold spraying

Xiawei Yang <sup>a</sup>, Tingxi Meng <sup>a</sup>, Yu Su <sup>a,\*</sup>, Zhiwei Qi <sup>a</sup>, Dong Wu <sup>a</sup>, Achilles Vairis <sup>a,b</sup>, Wenyu Li <sup>a</sup>

<sup>a</sup> State Key Laboratory of Solidification Processing, Shaanxi Key Laboratory of Friction Welding Technologies, School of Materials Science and Engineering, Northwestern Polytechnical University, Xi'an 710072, Shaanxi, PR China

<sup>b</sup> Mechanical Engineering Department, University of West Attica, Athens 12243, Greece

### ARTICLE INFO

#### Keywords:

Cold spraying  
Friction stir welding  
2219 aluminum alloy  
Microstructure  
Tensile strength  
Residual stress

### ABSTRACT

Friction stir welding is an advanced solid state welding technology, which has been widely used in aerospace and other fields. However, the large tensile residual stress developed in such joints will significantly affect mechanical properties. Cold spraying, as a new method to reduce residual stress of welded joints, can also improve the mechanical properties of the joints. In this paper, the correlation between microstructure and mechanical properties and residual stress of 2219 aluminum alloy joints prior and after coated with cold spraying was studied with experiments and numerical simulation for a 4 mm thick joint. The primary mechanism of stress relief of the joint was identified. Results show the refinement of grain size, with grain size decreasing from 2.1  $\mu\text{m}$  in welded joints to 0.7  $\mu\text{m}$  of cold sprayed joints, while high angle grain boundaries increase from 38.0% in the welded joint to 62.7% in cold sprayed ones. The ratio of recrystallized grains in the joints increases from 19.1% to 46.9%, while the joint strengthening phases  $\theta'$  and  $\theta$ ' increase, which increases tensile strength of the joints from 343 MPa to 398 MPa. The elongation is increased from 4.5% to 10.2%, and the average hardness of the joint is increased by 35 HV. The "shot peening effect" of cold spraying is found to be the primary factor to reduce residual stresses, while the "heat flow effect" has negligible effect on stress reduction. The mechanism of reducing residual stresses is provided by the macroscopic stress-strain theory and the microscopic dislocation theory.

### 1. Introduction

The 2219 aluminum alloy is a high-strength aluminum alloy that can be strengthened with heat treatment. It is widely used for fuel tanks of launch vehicles in aerospace due to its low density, high specific strength, excellent processing performance and corrosion resistance [1–3]. The techniques widely used to weld 2219 include electron beam welding (EBW), laser beam welding (LBW), variable polarity tungsten inert gas (VPTIG) welding, etc. [4–6], but the strength of joints produced with these fusion welding techniques can reach 50% ~ 70% of that of the base metal (BM). Moreover, joints are prone to cracks, pores and loss of alloying elements, with a poor performance of the joint [7–9]. Friction Stir Welding (FSW) is an advanced solid state welding technology developed by The Welding Institute in 1991 [10,11], which does not have the above common metallurgical problems of fusion welding. It is suitable for the welding of light metals and alloys of low melting point such as aluminum and magnesium, and has been widely used in the

welding of aluminum alloys in aerospace and other fields [12,13]. During welding, the weld material yields under the combined heat effects of friction and plastic deformation, producing adequate plastic flow. The metallurgical bond of the interface is produced from the extrusion action of the shoulder, thus forming a sound joint [14,15].

Studies have shown that residual stresses developed with FSW have an asymmetric distribution with longitudinal components [16,17]. These residual stresses affect mechanical properties, corrosion resistance and fatigue properties of joints. The deformation of the welded parts related to residual stresses may lead to assembly problems. Therefore, the reduction of residual stresses in FSW joints is of great interest to research. The widely used techniques to relieve residual stresses include thermal techniques (such as natural aging, heat treatment aging), mechanical techniques (such as shot peening, ultrasonic impact), and combination of thermal and mechanical techniques (such as laser impact). Nie et al. [18] studied the "shot peening effect" (SPE) on residual stress field of 2219 aluminum alloy used in a FSW joint.

\* Corresponding author.

E-mail address: [suyu0327@163.com](mailto:suyu0327@163.com) (Y. Su).



Results show that SPE can effectively reduce residual stresses, producing a compressive stress field on the joint surface. Huang et al. [19] found that ultrasonic impact produced extensive plastic deformation and residual compressive stresses on the surface of the joints when studies of ultrasonic impact treatment on corrosion fatigue performance of 2024-T4 aluminum alloy. For a corrosion time of 480 h, corrosion performance of the joint increased by 46.8%. The heat treatment techniques to relieve residual stresses require long process times with specific requirements for temperature and holding time, which may also cause oxidation of the weld. The vibration technique cannot be used for components in corrosive environments. Other methods such as laser impact have a significant effect on reducing residual stresses, but they are expensive to use. Therefore, there is a need for new techniques to reduce residual stresses of FSW welds.

Cold spraying (CS) is a technique that accelerates metal powder particles to velocities of 300–1200 m/s through specially designed Laval nozzle, which collides with a substrate in a solid state at low temperatures to produce large plastic deformation, and create a deposit [20]. In recent years, this technique has been widely used in aerospace, equipment parts, medical devices, and other fields for the production of functional coatings, repair damaged part surfaces, as well as for additive manufacturing [21]. Studies have shown that thermo-mechanical coupling effects (SPE and “heat flow effect”, HFE) do occur during CS, thus having the potential to relieve residual stresses in joints, and improve mechanical properties of them [22,23]. Li et al. [24] found that improving the distribution of residual stresses in FSW joints with CS improves fatigue life of parts, when investigating 2024 aluminum alloy joints. The compressive stresses produced by CS relieve partially the residual tensile stresses of the joint. The high temperature gas carrying the powder does assist with annealing the surface of the joints, relieving further residual stresses. Li et al. [25] studied the effect of CS on the residual stress field of 2219 aluminum alloy joints welded with VPTIG with a thickness of 8 mm which had large residual stresses from the large heat input of the welding technique. It was found that cold spraying relieved significantly residual stresses while producing a more uniform stress field. So, these show that cold spraying can relieve residual stresses in welded joints.

However, the mechanism through which CS relieves residual stresses remains to be investigated. Therefore, in this paper, the combination of experimental research and numerical simulation was used to study the effect of CS on the microstructure and properties of 4 mm thick 2219-T6 aluminum alloy joints produced with FSW. The effects of SPE, from the high-speed impact of powder particles, and HFE, from the high-temperature gas, on relieving residual stresses were studied separately. The mechanism for relieving residual stresses in FSW joints with CS has been described, in order to provide wider use of CS. The main innovation of this paper was the residual stresses could be significantly reduced by cold spraying, and the primary mechanism of stress relief of the joint was identified, providing theoretical basis and guidance for the follow-up research work.

## 2. Experimental procedure

### 2.1. Materials and methods

Sheets of 2219-T6 aluminum alloy with a thickness of 4 mm were selected as BM. Its chemical composition is shown in Table 1. The heat treatment state of T6 refers to artificial aging after solution treatment, under which the aluminum alloy has good plasticity and toughness [26].

Sheets with dimensions of 500 mm × 100 mm × 4 mm were butt-

welded with a rotational speed of 600 rpm, welding speed of 200 mm/min, and at a spindle inclination angle of 2.5°. The welding tool had a shoulder diameter, probe length and probe root diameter of 18 mm, 3.8 mm and 4.5 mm, respectively. Before welding, the surface of the joints was polished with sandpaper and cleaned with acetone. After welding, flashes were removed with polishing. The welded samples after polishing are shown in Fig. 1. Four joints were produced with FSW, where one weld was kept without any further processing, a second weld was coated with CS at a reduced gas temperature to study SPE, a third weld was put under the cold spraying machine without a powder at a high gas temperature to study the effects of HFE, and fourth weld was coated with CS. Residual stresses were measured in all four welds at the end.

The CS system was custom built in the Shaanxi Key Laboratory of Friction Welding Technologies of Northwestern Polytechnical University. A schematic diagram of the cold spraying of joints is shown in Fig. 2. Commercial spherical Cu powder with an average particle size of about 43.2 μm was used as the feedstock. During experiments, nitrogen was used as the gas medium, with spraying normally to the weld. The spray gun standoff distance from the joint surface was set at 30 mm. The traverse speed and powder feeding speed were set at 60 mm/s and 1.5 rpm, respectively. The CS parameters employed are shown in Table 2.

Samples for microstructural observation of 20 mm × 10 mm × 4 mm were cut perpendicularly to the welding direction. The specimens were ground with 280–5000 emery papers, mechanically polished, and etched with Keller's reagent (2.5 ml HNO<sub>3</sub> + 1.5 ml HCl + 1 ml HF + 95 ml H<sub>2</sub>O). The microstructure of the cross-section was studied with an optical microscope (OM, Keyence VHX-5000). Differential Scanning Calorimeter (DSC) measurements were taken with a differential synchronous thermal analyzer (NETZSCH STA449C) to identify precipitated strengthening phases for different conditions. From the temperature range for changing the strengthening phase of 2219, measurements were taken at a heating rate of 10 °C/min in the temperature range of 50–450 °C. The microhardness field of the joints was measured at a depth of 0.5 mm from the top surface of the joint with a Vickers hardness tester (LM248AT) with a load of 200 g and a dwell time of 15 s. The spacing between hardness measurements was of 0.5 mm. The tensile specimens were cut perpendicularly to the weld. The place from where specimens were cut from and dimensions of them are shown in Fig. 3a. The tensile strength tests were performed using an electronic universal testing machine (Instron 3382) at a rate of 1 mm/min. For each of the four welds the average tensile strength was measured. Residual stresses were measured with a HP-MK4 blind hole method residual stress device, seen Fig. 3b. The positions were to select five points from the advancing side (AS) to the retreating side (RS) of the weld for measurement, with a drilling diameter of 1.5 mm and a drilling depth of 2 mm.

### 2.2. Model and validation

Based on the Coupled Eulerian-Lagrangian (CEL) method, a geometric model was developed for the ABAQUS/Explicit solver, as shown

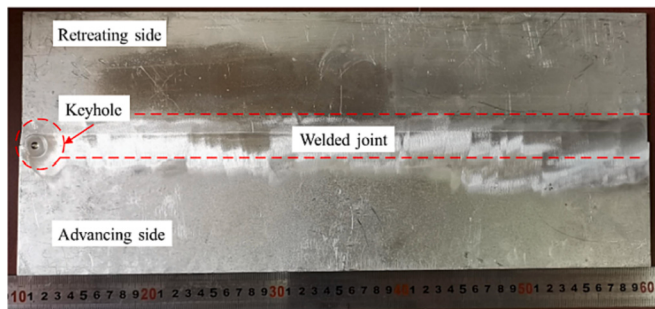


Fig. 1. Morphology of the joint.

**Table 1**  
Chemical composition of 2219-T6 aluminum alloy (wt%).

Si	Fe	Cu	Mn	Zn	Ti	V	Zr	Al
0.49	0.23	6.48	0.32	0.04	0.06	0.08	0.20	Bal

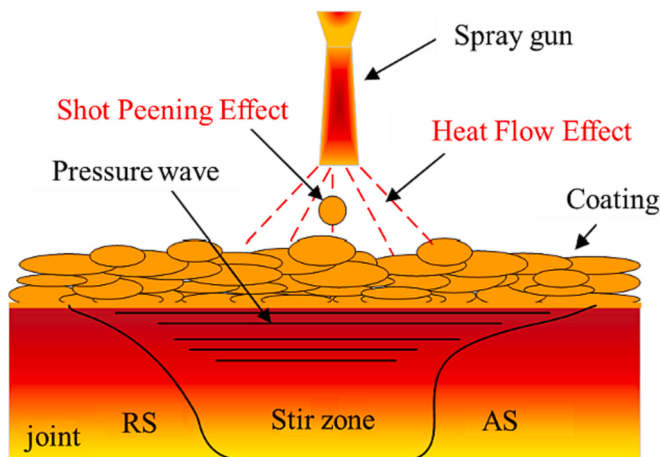


Fig. 2. CS on FSW joint surface.

**Table 2**  
CS parameters.

Sample	Gas temperature/°C	Gas pressure/MPa	Power
1 (SPE)	25	3	Cu
2 (HFE)	400	3	—
3 (CS)	400	3	Cu

in Fig. 4. The model consists of the weld (blue area shown in Fig. 4 represents the Euler space) and the welding tool. The dimensions of the weld model were 200 mm × 100 mm × 4 mm, with the weld located in the center. In order to accommodate the flash produced during the process due to pressure from the shoulder and rotation of the tool a layer of 1 mm thickness (grey area shown in Fig. 4) was created on top of the weld. The material properties were those of 2219 aluminum alloy, and the elements used were the EC3D8RT hexahedral grid type. The tool pin was made of H13 die steel with dimensions shown in Fig. 4. During modelling, it was regarded as a rigid body made of C3D8RT hexahedral grid elements. The element size of the weld and the tool pin was 0.5 mm, and the element size of the part away from the weld was 2 mm, producing 160,000 elements. The welding parameters of the numerical simulation were the same as in the experiments. In this model, the heat was generated by the friction between the shoulder, the tool pin and the BM. And five analysis steps were taken: tool press stage, tool rotation and dwell stage, welding stage, tool lift stage and fixture release stage, which were all set as thermos-mechanically coupled analysis steps of explicit dynamics.

The selection of the material constitutive model is critical to the

numerical model accuracy and reliability. The Johnson-Cook constitutive model is widely used for strain rate hardening, work hardening and high temperature softening effects in metals. It was selected as the numerical material model in this paper. In this model, the flow stress can be described with Eq. (1) [27]:

$$\sigma = (A + B(\varepsilon^P)^n) \left[ 1 + C \ln \left( \frac{\dot{\varepsilon}^P}{\dot{\varepsilon}_0^P} \right) \right] \left[ 1 - \left( \frac{T - T_{room}}{T_{melt} - T_{room}} \right)^m \right] \quad (1)$$

where A is the yield stress, B is the hardening modulus, C is the strain rate sensitivity coefficient, n is the strain hardening coefficient, m is the temperature sensitivity coefficient,  $\varepsilon^P$  is the equivalent plastic strain,  $\dot{\varepsilon}^P$  and  $\dot{\varepsilon}_0^P$  are the transient plastic strain rate and reference plastic rate.  $T_{melt}$  is the melting point,  $T_{room}$  is the reference temperature (room temperature). The parameters necessary for the Johnson-Cook constitutive model of 2219 aluminum alloy are shown in Table 3.

As FSW is a thermo-mechanically coupled process, material properties change with temperature, and in order to further improve the accuracy of the simulated residual stresses, these properties were calculated by JMatPro software, as shown in Fig. 5.

The boundary conditions set in the model include displacement and surface heat dissipation. As the boundary conditions of CEL cannot apply directly displacement constraints to the geometry boundaries, the model was instead constrained with velocity constraints to the corresponding

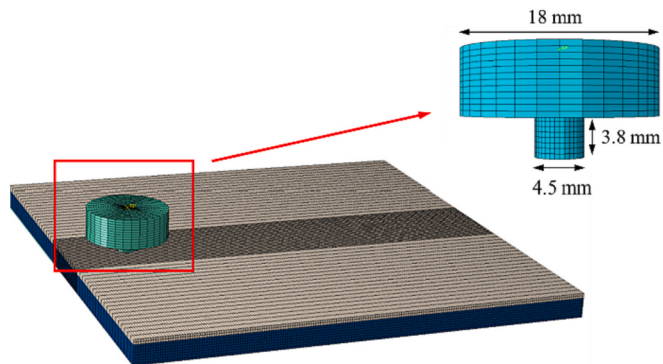


Fig. 4. Geometry, tool size and mesh.

**Table 3**  
Parameters of Johnson-Cook constitutive equation of 2219 aluminum alloy.

Material	A/MPa	B/MPa	C	n	m	T <sub>melt</sub> /K
2219	345	1100	1.5e-2	1	0.8	543

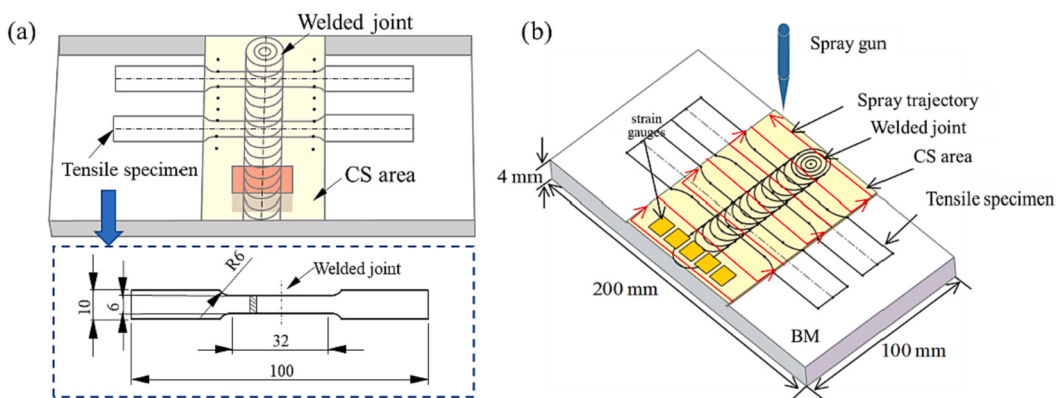


Fig. 3. Dimensions and position of the samples: (a) position and dimensions of tensile strength samples, (b) CS path and placement of strain gauges for residual stress measurement.

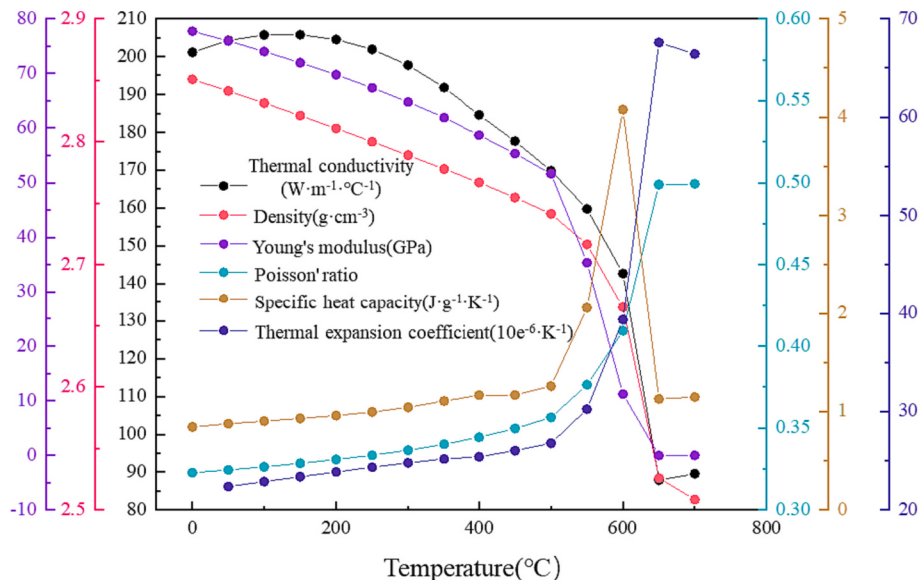


Fig. 5. Thermo-physical properties of 2219.

positions. Heat loss is performed through: heat conduction, heat radiation and convection heat transfer, all of which are temperature dependent. In order to simplify the model and improve efficiency, heat losses were simplified by ignoring conduction between the tool and the workpiece, while the heat convection coefficients between workpiece and backing plate or air were assumed to be  $1000 \text{ W}/(\text{m}^2\cdot\text{K})$  and  $35 \text{ W}/(\text{m}^2\cdot\text{K})$ , respectively [28]. These boundary conditions are shown in Fig. 6.

### 3. Results

#### 3.1. Temperature and microstructure of joints

##### 3.1.1. Temperature field

The temperature field in the steady state is shown in Fig. 7. It is symmetrical along the weld, with the maximum temperature area located in the shoulder-affected zone (SAZ). This is where the shoulder, tool pin and BM are under intense frictional heat generation and plastic deformation during welding, with friction action of the shoulder and the stirring action of the tool pin being the primary sources of heat generation in FSW.

The temperature gradient of the material located ahead of the tool tip is steeper than that after the tool tip, due to the  $2.5^\circ$  inclination angle of the tool. During welding, the material behind the tool undergoes intense frictional stirring action by the tool and heat conducted away from the subsequent welding, while the material at the front of the tool has not been mechanically stirred and conducts heat away solely from the tool tip. The temperature field (shown in Fig. 7b) shows a high-temperature

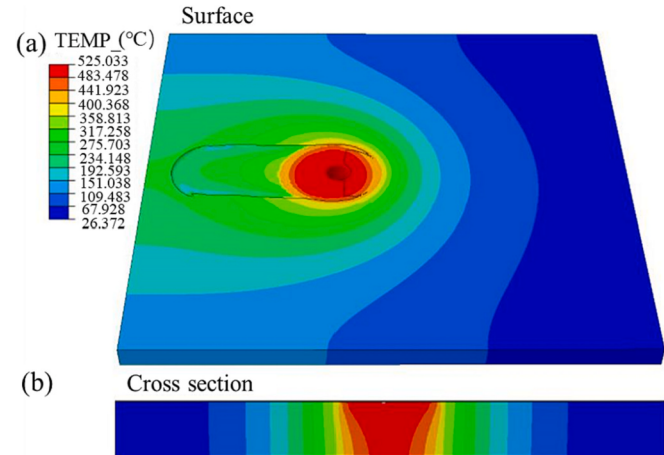


Fig. 7. Temperature field during steady state: (a) outer surface, (b) cross section.

area which has a “bowl” shape. The closer to the bottom of the BM, the narrower the high temperature area is. This is as the shoulder affects frictional heat generation, which has a stronger effect than the stirring effect on the material, while it is also related to heat conduction in FSW. During the welding process, the bottom of the BM is in contact with the backing plate and is rigidly fixed, and heat conduction between the metals is large, so the temperature of the bottom surface of the joint

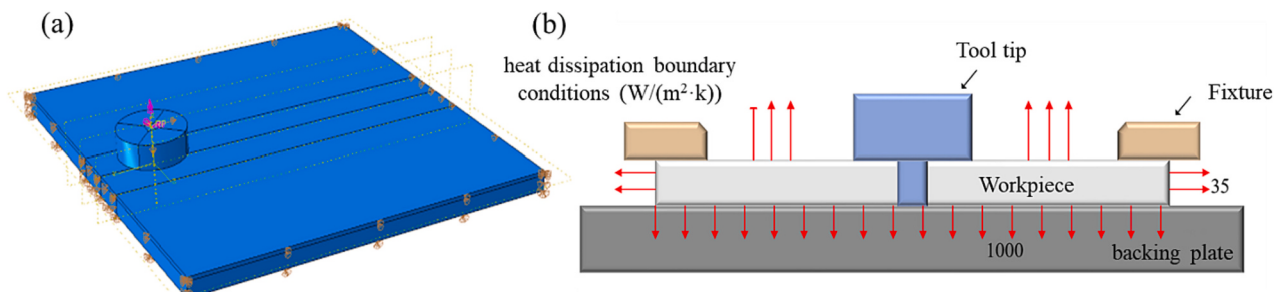


Fig. 6. Boundary conditions: (a) velocity, (b) heat losses.

being lower.

In addition, it can be seen from Fig. 7 that the maximum temperature in the weld in the steady state is 525 °C, which is lower than the melting point of the BM at 543 °C, therefore remaining in a solid phase. So, defects such as pores and cracks related to melting will not occur.

### 3.1.2. Microstructure analysis

The “shot peening effect” (SPE) and “heat flow effect” (HFE) were separately studied by performing experiments of two cases of “controlling the gas temperature at room temperature (1 #) “ and “without adding cold spraying powder (2 #) “. The microstructural changes of the four states of SPE, HFE, welded and CS joints (3 #) were analyzed, and the effect of CS on the microstructure of the joints was studied.

The morphologies of the joints in the four cases are shown in Fig. 8. It

can be seen that the joint is well formed after grinding, with no holes present and a solid joint. The cold spraying does not have good coating on the surface of the SPE joint. The SPE joint has only sporadic metal powder particles attached (as shown in Fig. 8d), but there appears plastic deformation due to high-speed impact of particles. Therefore, for good coating deposition temperatures and metal powder particles capable of adequate plastic deformation are required. The coating in the CS joint covers the entire weld in width and extends to the BM. The width of the CS area is about 70 mm. When N<sub>2</sub> is used as the working gas, the gas temperature and pressure are 400 °C, 3 MPa and when sprayed the coating thickness is about 500 μm. It can be seen from Fig. 8h that coating forms a good bond to the substrate, the coating is dense with low porosity, while there is clear plastic deformation at the interface between the coating and the joint substrate, as a result of the

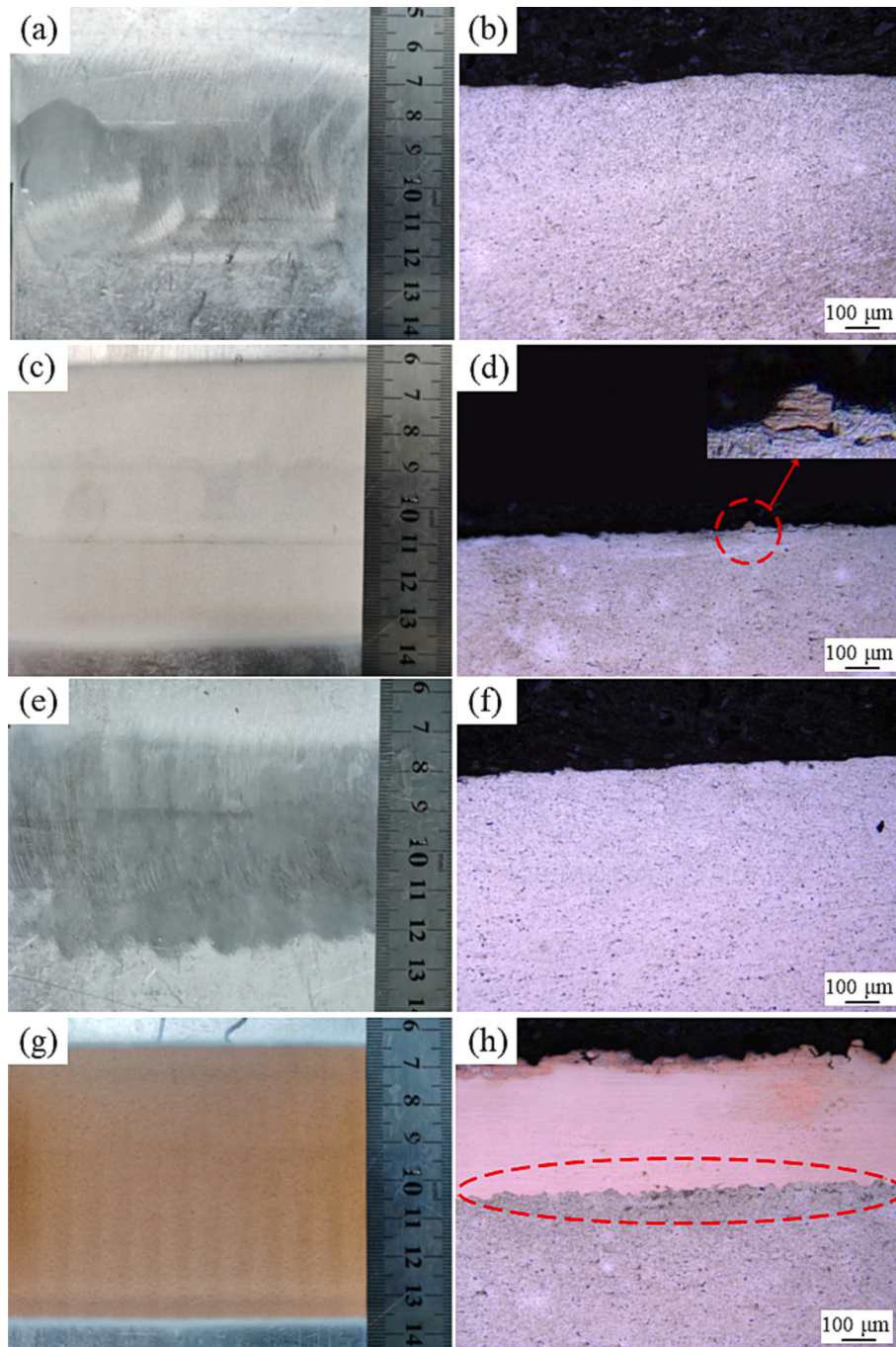


**Fig. 8.** Morphology of the joint at interface and cross-section: (a)(b) welded, (c)(d) SPE, (e)(f) HFE, (g)(h) CS.

high-speed impact of metal powder particles on joints during CS.

Fig. 9 shows the microstructure morphology of the joint after CS, where the main characteristics present in the FSW structure at the optical microscope scale remain the same. The stir zone (SZ) had refined grains with grain sizes ranging from 1 to 15  $\mu\text{m}$  due to dynamic recrystallization due to severe stirring of the tool pin and high frictional heat. Between the BM and the SZ is the thermo-mechanically affected zone (TMAZ) which has a highly deformed structure and elongated grains, which usually contain high-density sub-grain boundaries. The boundary between TMAZ and SZ on the AS is clear compared to that on the RS. The heat-affected zone (HAZ) is affected solely by heat, and has the same grain morphology and structure as the BM, showing a lath shape. However, due to the effect of temperature, grains grow and the strengthening phase coarsens compared to BM.

### 3.2. Effect of CS on microstructure of joint

In order to investigate further the effect of CS on the microstructure of the joints, and the relationship between microstructure evolution and residual stresses with joint properties, the electron back-scattered diffraction (EBSD) technique was used to scan the area 200  $\mu\text{m}$  from the center of SZ close to top surface of the four joints. The grain size, recrystallization degree and geometric necessary dislocations (GND) were measured.

Fig. 10 shows the IPF diagram and grain boundary angle distribution of the joint for the four cases. The black lines represent the high angle grain boundaries (HAGBs,  $\geq 15^\circ$ ), while the white lines indicate the low angle grain boundaries (LAGBs,  $2^\circ \sim 15^\circ$ ) in the images. It can be seen that grains close to the top surface of SZ also consist of fine equiaxed grains, which shows that CS does not affect grain morphology of the joint, but refines significantly grains. The average grain size measured with the intercept method in different cases corresponding to welded, SPE, HFE and CS were 2.1, 1.2, 1.3 and 0.7  $\mu\text{m}$ , respectively.

The refinement of SZ grains is due to the high-speed impact of metal powder particles on the surface of the joint during CS, which causes plastic deformation on the surface and refines the grains. The plastic deformation causes a large number of dislocations to accumulate in the grains, and dislocations are hindered by grain boundaries during movement and form dislocation pile-ups. As the dislocation density gradually increases, dislocations are entangled with each other to form a dislocation wall, which can then develop into subgrains. When deformation reaches a critical value, dislocations climb and slip, and transfer gradually to other boundaries of subgrains close to them, which merges adjacent subgrains. As dislocation increase in size and density, the orientation difference of adjacent subgrains also increases and gradually transforms into HAGBs. Fig. 10b, d, f and h show the proportion of HAGBs close to the top surface area of SZ for the four cases of joints. The proportion of HAGBs in the CS joint (62.7%), SPE joint (55.0%) and HFE

joint (52.3%) is significantly increased compared to that of the weld (38.0%). The HAGBs have a much larger mobility than the LAGBs, with dislocations removed during movement. Finally, as HAGBs develop the original grains become finer with random orientation. The whole process produces an increase of dislocation density, dislocation tangling, dislocation wall, subgrain, HAGBs and grain refinement.

At the same time, because of high temperature gas of cold spraying, the surface temperature in the joint reaches the recrystallization temperature range of 2219 aluminum alloy. So, dynamic recrystallization of SZ grains occurs during CS, and grains refine. In order to describe quantitatively the recrystallization degree of the joint during CS, Fig. 11 shows the recrystallization distribution maps and ratios for the four cases. It can be seen that there are more deformed grains (40.7%) and fewer recrystallized grains (19.0%) in the joint, due to the strong mechanical stirring action of the tool while a limited number grains recrystallize from heat input during welding of the SZ. In the case of the SPE joint, metal powder particles at room temperature impact on the substrate, and no dynamic recrystallization occurring, the ratio of deformed grains in the joint increases (43.1%). The ratio of recrystallized grains in the CS joint and the HFE joint increased significantly (CS: 46.9%, HFE: 30.9%) when the temperature of the cold spray gas matches the recrystallization temperature range of the joint material.

The 2219 aluminum alloy is a face-centered cubic metal with high stacking fault energy. Due to the small width of the extended dislocation, it is easy to produce cross-slip. With increasing strain during CS, a large number of dislocation walls formed by entanglement will undergo continuous dynamic recrystallization, and LAGBs will form through cross-slip arrangement and combination. As grain boundary orientation differences increase, they gradually transform into HAGBs. This dislocation interface, formed by cross-slip, continuously forms and divides into grains to refine them. The refined grains produced by plastic deformation and dynamic recrystallization during CS and the high ratio of HAGBs are the key to improve mechanical properties of 2219 aluminum alloy joint.

From the analysis above, it can be seen that dislocations inside grains and changes in dislocation density are critical for improving the properties of the joint during CS. In order to quantitatively study the effect of CS on the geometrically necessary dislocations (GND) of the joints, the distribution of GND in SZ grains was related to local misorientation distribution. The homogenization of plastic deformation of metals can be associated with the local misorientation difference inside the part. The lighter color region indicates a high degree of plastic deformation and dislocation density. The local misorientation difference of a point is determined by the misorientation difference of 24 points next to it [29]. In order to ensure the accuracy of statistical calculation, points with local misorientation difference  $>2^\circ$  are excluded from calculations. The average misorientation difference at this position can be calculated with Eq. (2):

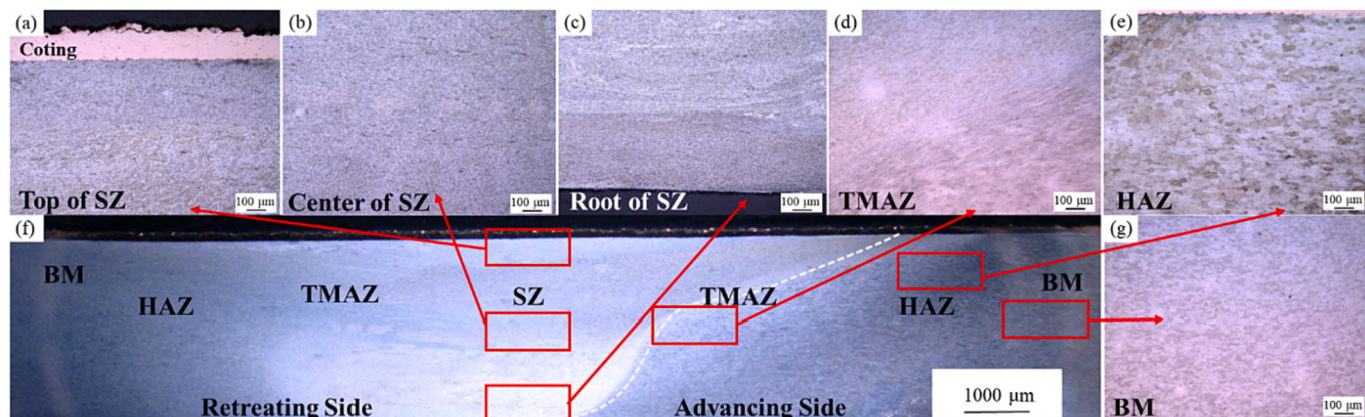
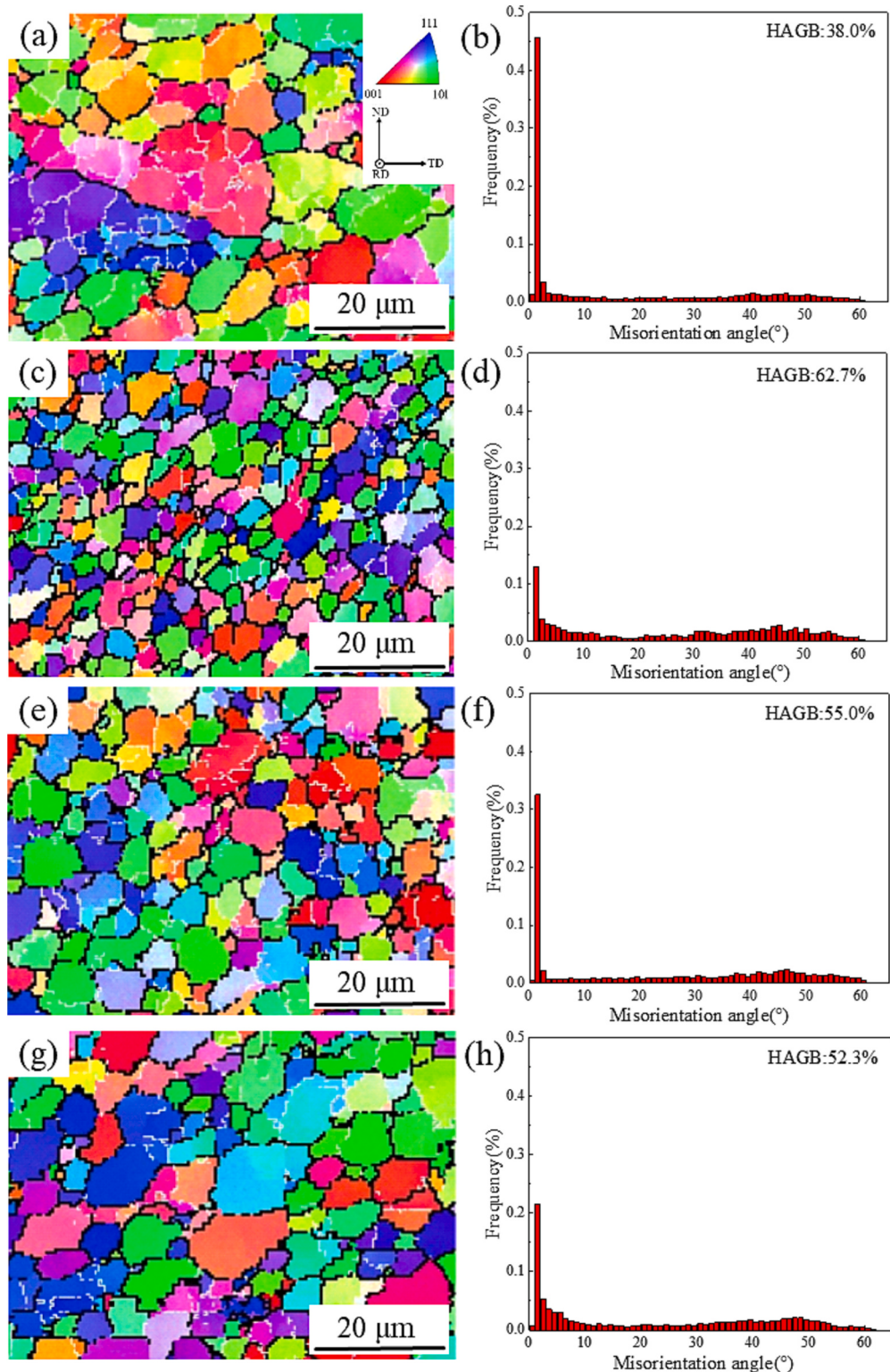


Fig. 9. Structure of the cold sprayed joint.



**Fig. 10.** IPF maps and misorientation angle distribution in SZ of the joints: (a)(b) welded, (c)(d) CS, (e)(f) SPE, (g)(h) HFE.

$$\Delta\theta_i = \frac{1}{n} \sum_{j=1}^n |\theta_j^{sur} - \theta_i| \quad (2)$$

$$\rho^{GND} = \frac{2\Delta\theta_i}{\mu b} \quad (3)$$

where  $\theta_i$  is the local misorientation difference at  $i$ ,  $\theta_j^{sur}$  is the local misorientation difference of adjacent point  $j$ . The calculation method of strain gradient model [30] is used to calculate the GND density of the target area, and Eq. (3) is as follows:

where  $\mu$  is the analysis step length used in the EBSD measurements ( $0.4 \mu\text{m}$  was used), and  $b$  is the Burgers vector length ( $2.86 \times 10^{-10} \text{ m}$  was selected). The data from the local misorientation distribution map produced EBSD can be used as angle  $\theta_i$  for this calculation. Fig. 12 is the

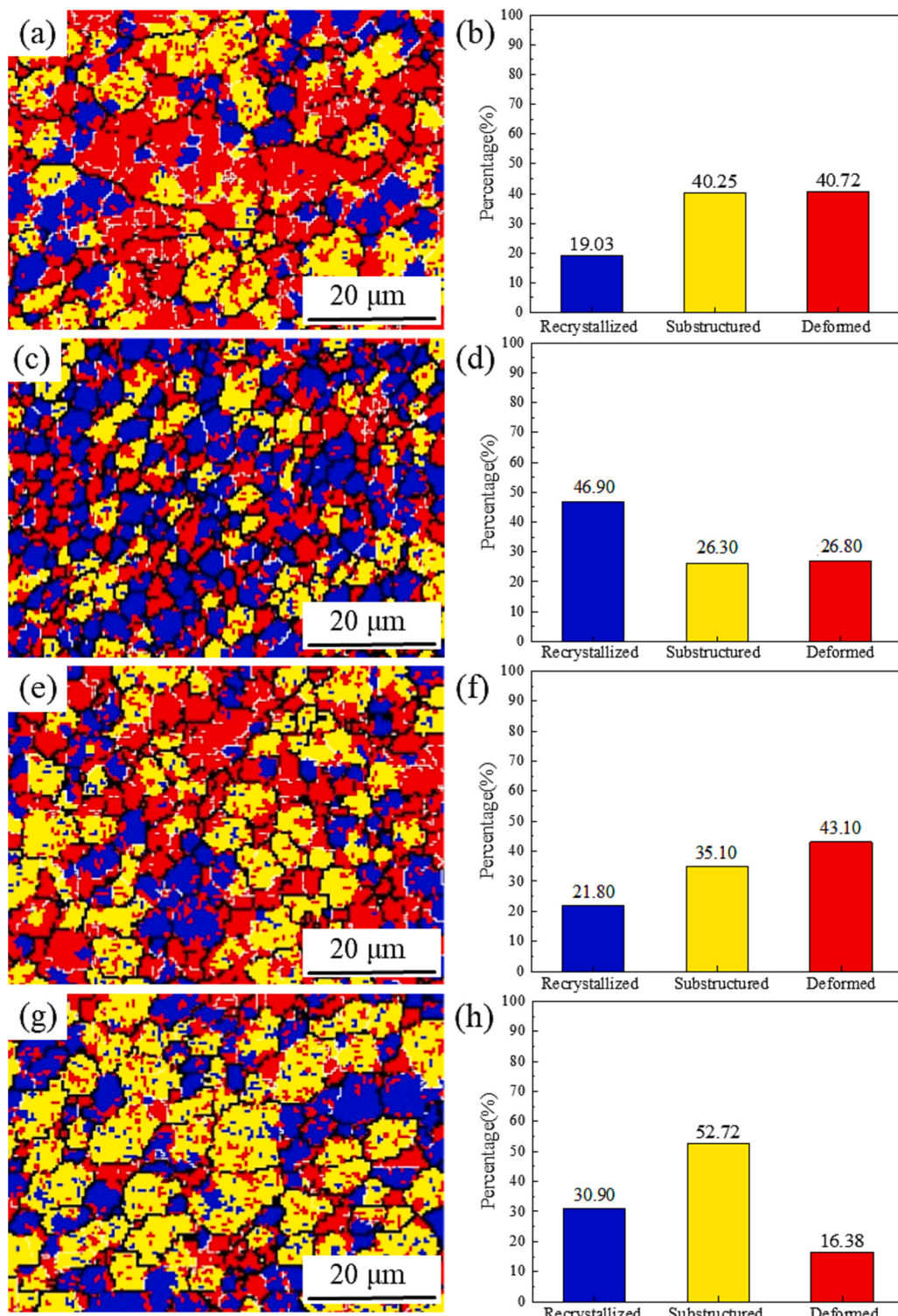


**Fig. 11.** Distribution diagram of recrystallization in SZ of the joints: (a)(b) welded, (c)(d) CS, (e)(f) SPE, (g)(h) HFE.

local misorientation distribution map and statistical map of the joint for the four cases.

The statistical analysis of the local misorientation difference in Fig. 12 shows that the  $\Delta\theta_i$  of the four joints is  $0.192^\circ$  for the welded joint,  $0.194^\circ$  for the CS joint,  $0.22^\circ$  for the SPE joint and  $0.2^\circ$  for the HFE joint, respectively. The GND density for each joint is calculated with Eq. (3) to be  $3.36 \times 10^{15} \text{ m}^{-2}$ ,  $3.39 \times 10^{15} \text{ m}^{-2}$ ,  $3.85 \times 10^{15} \text{ m}^{-2}$  and  $3.50 \times 10^{15} \text{ m}^{-2}$ , respectively. It can be seen that the GND of the SZ region on the top surface of the joint increases after CS. This is the result of plastic

deformation caused by the high-speed impact of metal particles on the surface of the joint during CS.

From these calculations, it can be seen that the GND density of the CS joint and the HFE joint is not much higher than that of the SPE joint. This relates to the heat input of the cold spraying gas, which allow grains to recover dynamically and recrystallize dynamically. In addition, a higher ratio of HAGBs will also absorb and remove dislocations during their movement, which reduces dislocation density. The diagram shows that plastic deformation in the welded joint is not uniform, with local

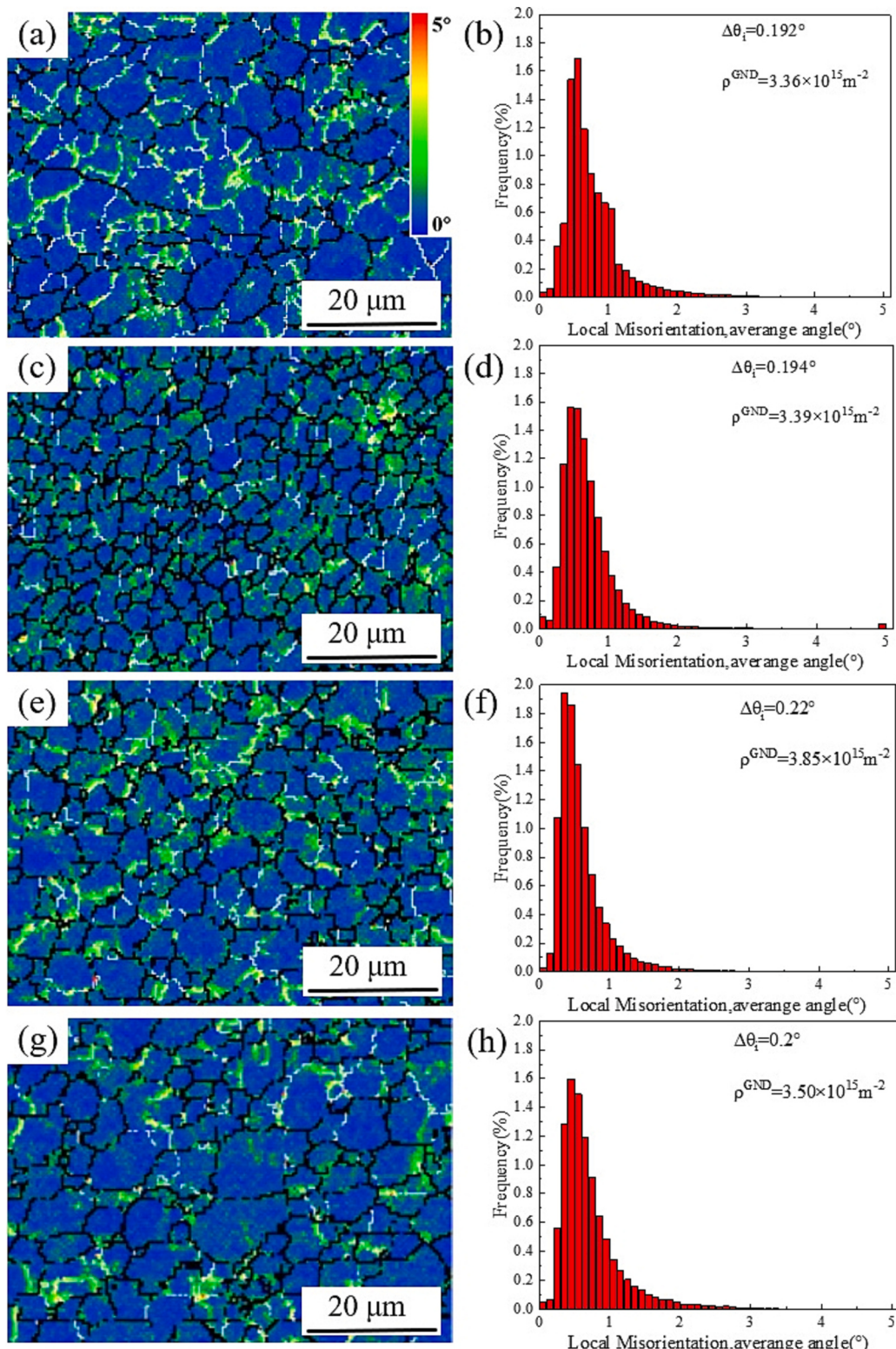


Fig. 12. Local misorientation maps in SZ of joints: (a)(b) welded, (c)(d) CS, (e)(f) SPE, (g)(h) HFE.

misorientation difference being very large in certain areas (green bright area in Fig. 12a), as lattice distortion in increased and stress is concentrated in this position. While the three joints treated with CS show a high dislocation density, the overall distribution is uniform and lattice distortion is low, as CS reduces locally the maximum residual stress.

## 4. Discussion

### 4.1. Effect of CS on phase transformation

The 2219 aluminum alloy is an Al–Cu heat-treatable high-strength alloy, and during aging dissolution the order is from supersaturated solid solution to GP zone (Cu atom cluster, coherent), then to  $\theta''$  phase ( $Al_2Cu$ ,

coherent), followed by  $\theta'$  phase ( $\text{Al}_2\text{Cu}$ , semi-coherent), to reach  $\theta$  phase ( $\text{Al}_2\text{Cu}$ , incoherent). The primary strengthening phases are the  $\theta''$  and  $\theta'$  phases. The change of properties is related to the interaction between strengthening phases and dislocations. The interaction of coherent strengthening phase GP zone and  $\theta''$  phase with dislocation is the switching mechanism, as shown in Fig. 13a. When the dislocation runs into the strengthening phase deforms the precipitated phase particles, which increases the interface area between the precipitated strengthening phase and the aluminum matrix. The interface energy increases, which distorts the lattice of the aluminum matrix, and hinders dislocation movement in the crystal, which in turn increases strength and hardness of the 2219 aluminum alloy. When the semi-coherent  $\theta'$  phase is further precipitated, the strength and hardness will increase further as well. When the incoherent stable  $\theta$  phase begins to precipitate, the dislocation bypasses the  $\theta$  phase particle, deteriorating the properties of 2219 aluminum alloy (Fig. 13b). The changes of the strengthening phase precipitated prior to and after welding as well as during CS is the main reason for various properties changes in the joints.

Fig. 14 shows the DSC curves of the BM and the top surface material of SZ of the four joints. The endothermic and exothermic maxima identify the dissolution and precipitation of various precipitated phases. The larger the area under the maximum, the higher the content of the precipitated phase. From the precipitation phase transition diagram for 2219 aluminum alloy, the precipitation phases related to different maxima were identified. In Fig. 14, the exothermic maximum in area I ( $100\text{--}150^\circ\text{C}$ ) was the precipitation maximum of GP region, and the endothermic maxima in area II ( $225\text{--}275^\circ\text{C}$ ) and area III ( $275\text{--}300^\circ\text{C}$ ) were related to the dissolution of  $\theta''$  and  $\theta'$  phases. From Fig. 14, there appears to be  $\theta'$  strengthening phase only present in BM, and the area over the endothermic maximum of the BM is larger than that of the other four cases, a difference matching with improvement in mechanical properties. This relates to the fact that the aluminum alloy used in this study is in the T6 state (artificial aging after solid solution heat treatment), with an increased number of dislocations and improved mechanical properties. During welding, heat generated by the shoulder and the tool pin, increases temperatures locally and dissolves back the

strengthening phase, thus forming a supersaturated solid solution. In addition, cooling after welding is similar to natural aging, and solute atoms precipitate from the aluminum matrix again. It can be clearly seen from the Fig. 14 that the welded joint has GP zone,  $\theta''$  and  $\theta'$  phases. The application of CS, shows that the precipitation maxima of the GP zone in the CS joint and the HFE joint disappear, while the precipitation maximum of the GP zone in the SPE joint still remains, but with a lower content than that of the welded joint. This is because CS increases the temperature of the joint again followed by cooling, similar to an aging treatment, as the GP zone of the welded joint transforms into strengthening phases  $\theta''$  and  $\theta'$ . The SPE joint was processed at room temperature, with a limited quantity of heat generated by plastic deformation of a few powder particles, making the size of the GP zone negligible to that of the welded joint. The content of both strengthening phases  $\theta''$  and  $\theta'$  in the SPE joint were lower than that of the HFE joint. While the CS joint is exposed to the thermo-mechanical effects of the process, the  $\theta''$  and  $\theta'$  phases are increased than that of the welded, SPE and HFE joints, which affects similarly strength and hardness.

#### 4.2. Effect of CS on mechanical properties and residual stresses

##### 4.2.1. Microhardness

Fig. 15 shows the microhardness measured near the top surface for each of the four joints, which is related to the microstructure present. The lowest hardness appears near the TMAZ on the AS. The hardness in the HAZ-TMAZ is lower compared to that of the BM. In the SZ, hardness increases due to the pressure applied by and the high-speed rotation of the tool pin. Both CS and SPE joints possess a significantly higher hardness are than that of the welded joints (the average hardness value increases by 35 HV and 28 HV, respectively), while the overall trend remaining unchanged, which relates to the high-speed impact of powder particles on the surface of the substrate. The SPE shows a work hardening effect on the surface of the joint. The fine grain strengthening effect of CS on the joint contributes to the increase in microhardness. The relationship between microhardness and grain size is described by the Hall-Petch formula [31]:

$$Hv = Hv_0 + K_{Hv}d^{-1/2} \quad (4)$$

where  $Hv$  is the microhardness,  $Hv_0$  and  $K_{Hv}$  are constants related to microhardness, and  $d$  is the average grain diameter.

In addition, residual stresses on the surface of the part affect microhardness, a matter which will be discussed later in the paper. From Fig. 15, it can be seen that the hardness of the HFE joint is similar to that of the welded joint, while BM has lower hardness than that of the welded joint and the hardness of the SZ increases. Prior research conducted by our research group indicates that [24]: the HFE during the CS can partially transform the solute atom group in the 2024 aluminum alloy matrix into the S phase ( $\text{Al}_2\text{CuMg}$ ), and the gas temperature during the CS will not coarsen the S phase and cause hardness will not decrease. Moreover, it can be seen from the previous analysis that the HFE during CS increases the content of the strengthening phases  $\theta''$  and  $\theta'$ , which is also the reason for the increase in hardness of the SZ.

##### 4.2.2. Tensile strength

In order to study the effect of CS on strength and plasticity of the joints, the tensile strength of the four joints was measured. Fig. 16a shows the engineering stress-strain curves of the four joints. The ultimate tensile strength (UTS) and elongation (EI) are shown in Fig. 16b.

Fig. 16 shows that the tensile strength of the joint following CS is improved, with the UTS increasing from 343 MPa to 398 MPa, an increase of 16%, as CS has a significant effect on the improvement of the elongation of the joint, which is increased from 4.5% of the welded joint to 10.2%, an increase of 126%. Although the UTS and EI of the SPE and HFE joints are higher than those in the welded joint, the improvement of the tensile strength in the SPE joint is higher than that in the HFE joint

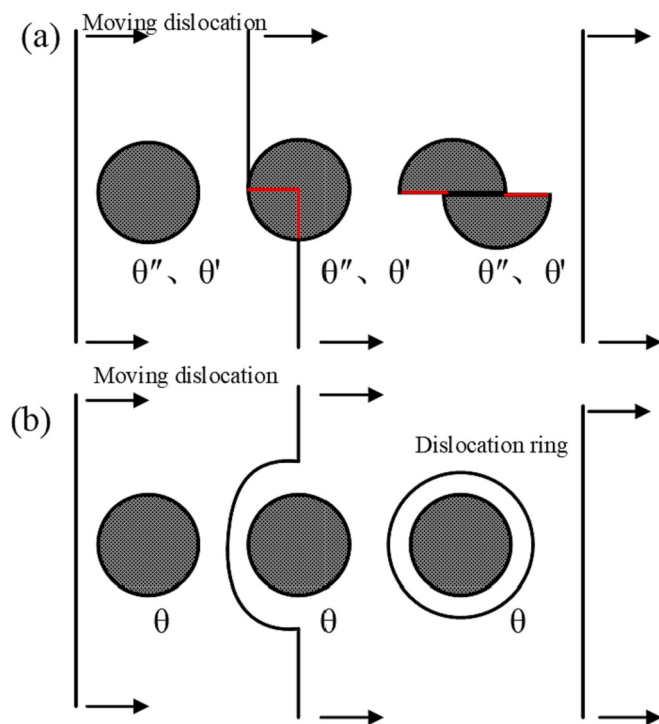


**Fig. 13.** Interaction between 2219 aluminum alloy precipitates and dislocations: (a) switching mechanism, (b) bypass mechanism.

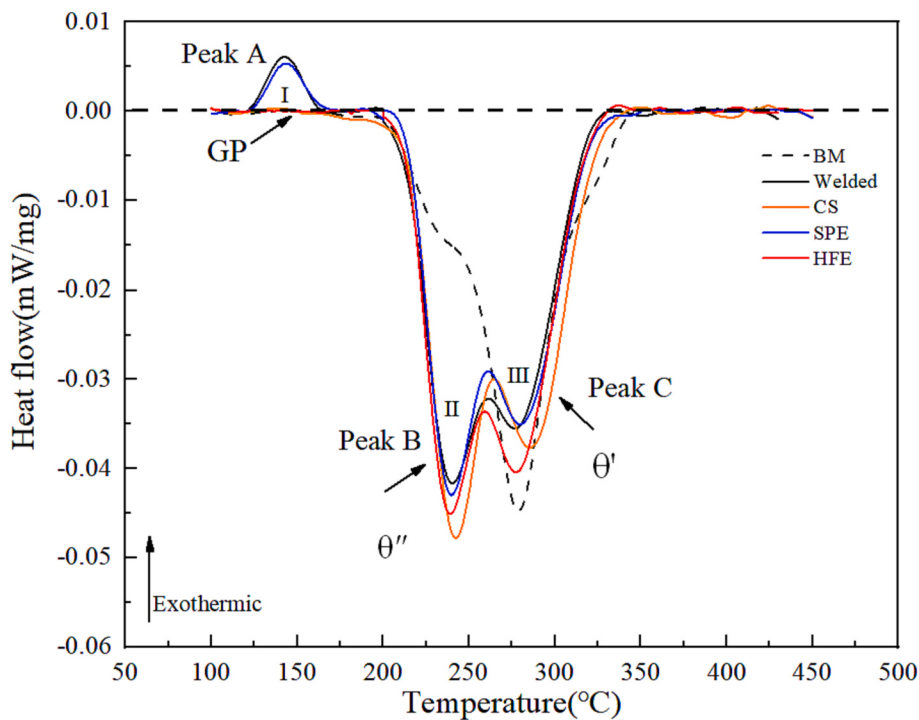


Fig. 14. DSC curve of SZ top surface of joints.

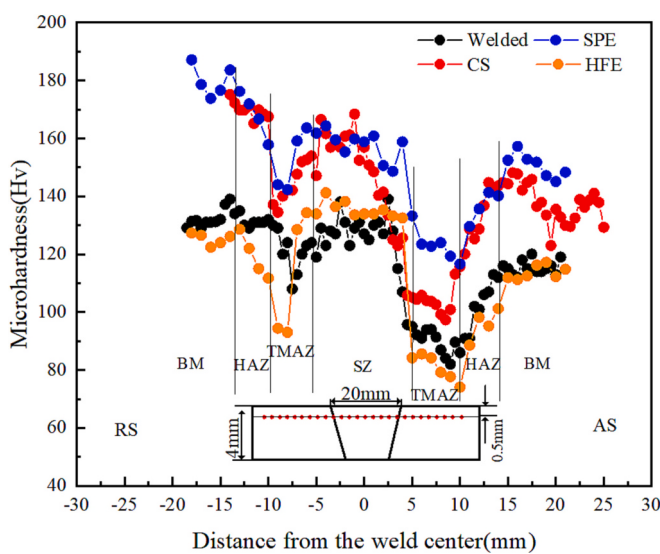


Fig. 15. Microhardness near the top surface of joints.

(SPE joint: 384 MPa, HFE joint: 377 MPa), while the HFE joint has a higher increase of the EI (from 4.5% in the welded joint to 11.4%), which shows that SPE and HFE affect strength and plasticity of the joints in a different manner CS. The high-speed impact of metal powder particles produces grain refinement of the surface of the SPE joint. The fine grains hinder dislocation movement, and the slip amount is dispersed in each grain, resulting in limited stress concentration which does not allow cracking. Therefore, fine grain strengthening of the SPE joint can simultaneously improve strength and plasticity. From the analysis above, the dynamic recrystallization of the surface material of the HFE joint occurs because of gas temperature, and the ratio of HAGBs increases. The HFE increases the content of the strengthening phases  $\theta''$  and  $\theta'$ , and the tensile strength of the joint improves by precipitation strengthening.

It can be seen from Fig. 17b that following CS, coating has peeled off during the tensile strength testing. The fracture of the joint is near the interface of the TMAZ and the HAZ on the AS, and both are broken at an angle of 45°. This is consistent with the location of the low hardness region in Fig. 15. The fracture surface morphology of the four joints is shown in Fig. 17, which are typical of plastic fracture with a large number of dimples and tearing ridges, and there is a large number of dispersed second phase particles found in the dimples, which is  $\text{Al}_2\text{Cu}$  as identified by EDS.

#### 4.2.3. Residual stresses

Published literature shows that residual stresses are primarily longitudinal stress, with transverse stresses remaining small [32,33]. So, longitudinal residual stresses will be investigated in this paper. Fig. 18a shows residual stresses in the joint. It can be seen that residual stresses in the welded joint have two maxima and they are tensile stresses. The maximum value is located at the boundary of the TMAZ and the HAZ of AS, at 132 MPa, to decrease afterwards. This is due to uneven heat input and mechanical stirring during FSW. During the welding, the longitudinal tensile stress continues to increase and increases further with cooling after welding. The material on the RS is under longitudinal compression during welding, and residual stresses are slightly lower. This creates an asymmetric residual stress field across the weld, and a residual stress maximum is observed at the AS, which is typical of FSW longitudinal residual stresses. The residual stress calculated by simulation is compared to the value measured with the blind hole method, and results are shown in Fig. 18b. The calculated residual stresses are higher than those measured. It may be due to the cutting and grinding of the weld during measurement, which material removal releases residual stresses to an extent. The simulated residual stress maximum on the AS is 139 MPa, while those measured are 132 MPa. The simulated residual stresses of the RS are 130 MPa, while those measured are 99 MPa, producing an error of 23%. The morphology of the cross section of the joint is compared to the calculated equivalent plastic strain of the weld. It can be seen that the model can accurately predict the size and shape of the plastic strain zone of the weld.

From Fig. 18a, it can also be seen that residual stresses of CS and SPE

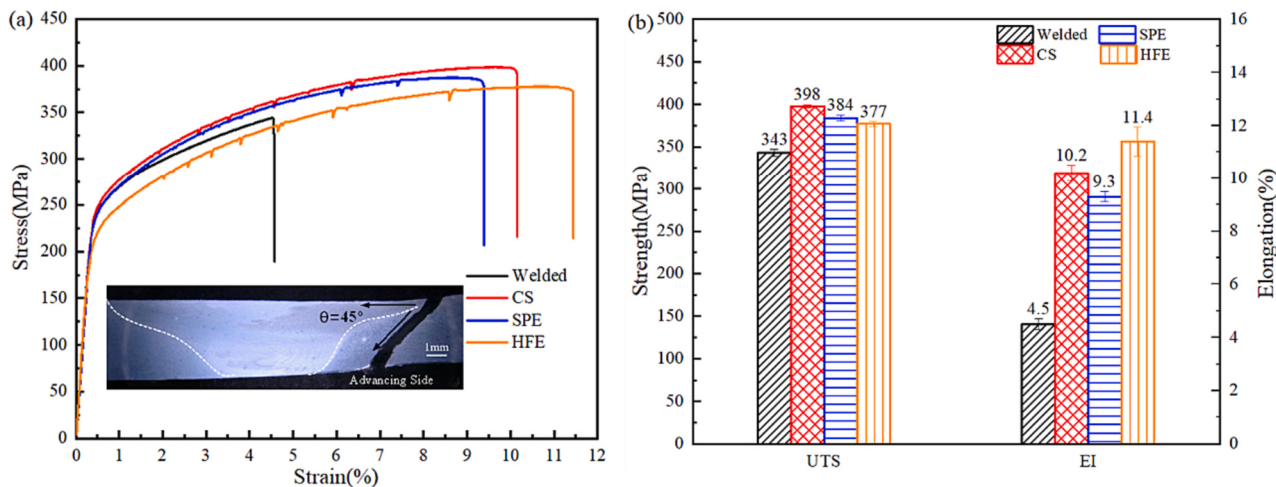


Fig. 16. Tensile strength of joints: (a) engineering stress-strain curves, (b) UTS and elongation.

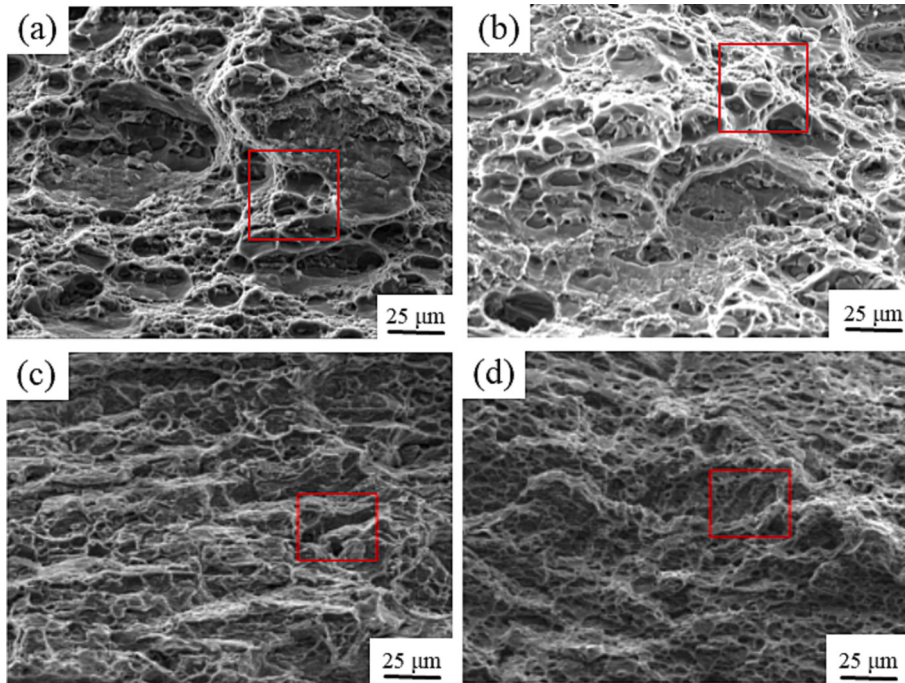


Fig. 17. Fracture surfaces of joints: (a) welded, (b) CS, (c) SPE, (d) HFE.

joints are significantly lower than that of the welded joints. The maximum residual stress on the AS of CS joint is reduced from a tensile stress 132 MPa to compressive stress 17.4 MPa. The overall stress distribution is relatively uniform, with no maxima. The overall residual stress of the HFE joint is similar to that of the welded joint, but the asymmetric change of residual stresses with two maxima is uniformly distributed, which reduces stress concentration on the AS of the joint. So, SPE is the primary factor to reduce residual stresses in the joint, while HFE can produce a uniform overall stress distribution. During CS, powder particles at low temperature and high speed continue to impact the weld surface, producing large plastic deformation. The continuous impact of high pressure gas, produces large compressive stresses on the surface of the joint, which is added to the residual tensile stresses of the FSW joint itself, which reduces overall residual tensile stresses and changes them compressive. The mechanism of CS to reduce the residual stresses will be described later in the paper. From published literature [34–36], the development of residual tensile stresses on the surface of

the substrate, decreases hardness, while compressive stresses increase hardness. Because of the particular characteristic of CS which reduces asymmetric residual tensile stresses and transforms them into compressive stresses in parts, which increases microhardness of CS and SPE joints.

The primary reason for producing residual stresses in FSW is the uneven plastic deformation of the BM, which relates to the intense mechanical stirring by the tool pin and the presence of plastically deformed areas next to areas which are not plastically deformed.

The approach to improve and reduce welding residual stresses can be: either to reduce elastic strain inside the part, or, following the theory of minimum energy. In the first case, external loads (heat, forces, etc.) are applied to the material, deforming it plastically in part, and reducing elastic stresses inside the part, and decreasing overall residual stresses. In this manner, if elastic strains are totally transformed into plastic strains, residual stresses can be completely eliminated under ideal conditions. If they are partially transformed, then residual stresses will

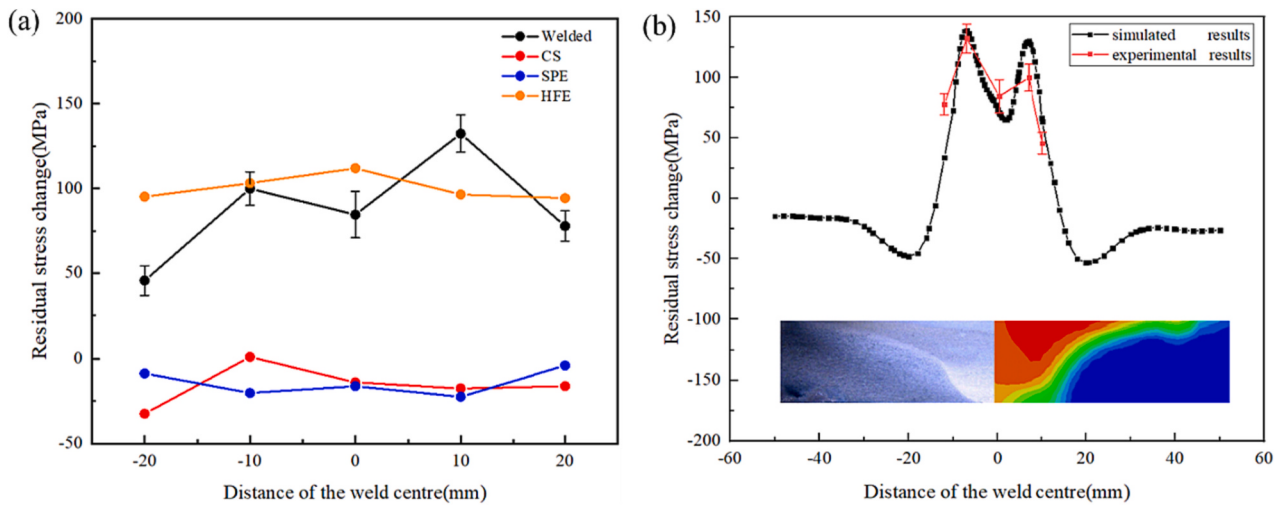


**Fig. 18.** Residual stresses: (a) residual stresses on joint surface, (b) experiments and simulation comparison of residual stresses.

reduce accordingly. The second technique extracts energy by making the atom deviate from its equilibrium position, so that they return from the position with higher energy to the equilibrium state, this reducing total energy reduced, and reducing lattice distortion, and improving residual stresses. The CS combines these two techniques to reduce residual stresses of FSW joint.

From macroscopic stress-strain theory, in order for CS to reduce residual stresses, the sum of the residual stresses produced by welding together with the impact force that the metal powder particles strike the substrate surface must be over the yield limit of the material. The necessary condition for CS to reduce the residual stress after welding can be expressed by Eq. (5) [37]:

$$\sigma_{cs} + \sigma_r \geq \sigma_s \quad (5)$$

where  $\sigma_{cs}$  is the stress generated by impact on the surface of the joint,  $\sigma_r$  is the residual stress of the joint,  $\sigma_s$  is the yield point.

When the Eq. (5) holds, the high-speed impact of metal powder on the surface of the substrate during the CS yields material locally at the maximum value of the residual stress, which then produces plastic deformation. The maximum value will decrease to a uniform stress distribution. When the residual stress of the joint is reduced to a certain level, and the sum of  $\sigma_{cs}$  and  $\sigma_r$  is lower than  $\sigma_s$ , material will not deform plastically anymore, and the joint will remain at a steady stress state.

The HFE of the gas during CS will also annealing locally the surface of the joint. The increase in surface temperature during CS reduces yield strength and elastic modulus [26]. This reduction allows for further plastic deformation when impact occurs, and residual stresses decrease as well. So, the higher the gas temperature, the stronger residual stress reduction will be. But, HFE in CS is not equivalent to conventional heat treatment to reduce residual stresses. Heat is not conserved, and the cooling rate is quick and uneven. The higher temperature may also introduce thermal stresses, which increase the residual stresses in the joint.

Based on microscopic dislocation theory, residual stresses are because of the uneven distribution of lattice distortion, with lattice distortion being affected by dislocations. Plastic deformation of the material is actually the slip of dislocations on the slip surface. When dislocation movement is hindered and cannot complete on the slip surface, they pile up inside the grain, which distorts the lattice. The dislocation pile-up produces stress concentration, which when increased over a limit, it will force dislocation movement from adjacent grains, which will produce slip, relaxing stress concentrations and opening up pile-up. If dislocation pile-up cannot be relaxed, microcracks will occur and lead to fracture. The strong stirring effect of the tool pin produces

uneven plastic deformation, which keeps a large number of dislocations to stay inside grains. The dislocation pile-up will form a complex elastic stress field (dislocation pile-up stress field). The opening of dislocation pile-up can reduce lattice distortion and release residual stresses in the joint. The dislocation pile-up stress field  $\tau$  is used to represent its force to adjacent dislocations [37].

$$\tau \approx \frac{4}{\pi} \left( \frac{L}{r} \right)^{\frac{1}{2}} \tau_0 + \tau_0 \quad (6)$$

where  $\tau_0$  is the external shear stress,  $r$  is the distance from the adjacent dislocation to the dislocation pile-up,  $L$  is the total length of dislocation pile-up group.

When the shear stress  $\tau$  is large enough to overcome the resistance of dislocation movement, the dislocation source will continue to release dislocations, the grain will yield plastically, the lattice distortion will be reduced, and the stress concentration will be reduced. When dislocation moves from one grain to another, the internal stress is relaxed.

The SPE of the CS will also deform plastically the surface, with a large number of dislocations generated inside the grains, which result in dislocation pile-up. Therefore, during reducing residual stresses in FSW joints with CS, the shear stress  $\tau$  that moves adjacent dislocations consists of two parts: the first one is the stress field where the residual stress of the joint itself is in the dislocation pile-up, expressed as  $\tau_r$ . The greater the residual stress, the greater the lattice distortion, and therefore the greater the corresponding  $\tau_r$ . The other part is the stress field created by the dislocation pile-up, created from the CS, expressed as  $\tau_{cs}$ . The stress due to plastic deformation from one grain to another is  $\tau_s$ , which equals to the yield strength of the material. The microscopic necessary condition for CS to reduce the residual stress of the FSW 2219 aluminum alloy joint can be expressed as Eq. (7) [37].

$$\tau_{cs} + \tau_r \geq \tau_s \quad (7)$$

This agrees with Eq. (5) of CS to reduce residual stresses as described by the macroscopic stress-strain theory. From Eq. (7), the increasing dislocation pile-up stress field  $\tau$  can make dislocations move to another grain and let dislocation pile-up open (as shown in Fig. 19). For the same applied shear stress  $\tau_{cs}$ , the dislocation pile-up stress field  $\tau_r$ , generated by the primary lattice distortion, is superimposed on  $\tau_{cs}$ , which applies larger force on the adjacent grain dislocation, so the dislocation pile-up opens up. Actually, the maximum value of residual stresses in the FSW joint is initially relaxed during CS. If stresses, after the superposition of  $\tau_{cs}$  and  $\tau_r$  two, remain low, then it does not allow dislocation movement in adjacent grains, which brings an equilibrium state for dislocation pile-up. In areas with lower lattice distortion then residual stresses are low.

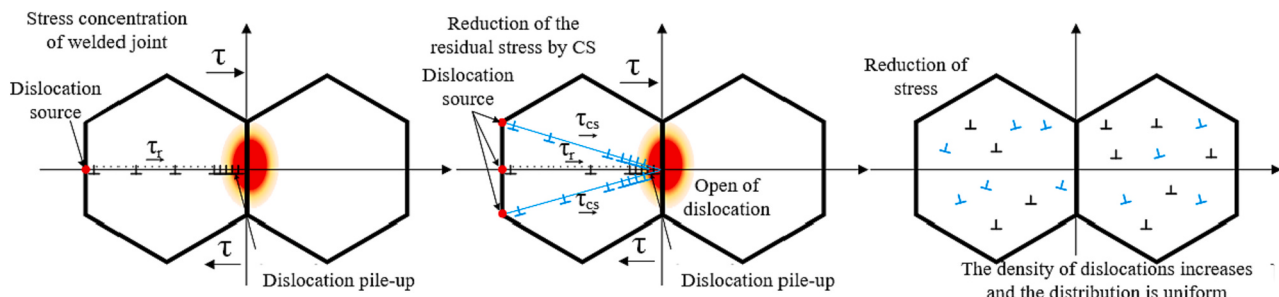


Fig. 19. Dislocation model for reducing residual stresses with CS.

As dislocation and dislocation pile-up generated by CS distort the lattice, residual stresses in these areas joint increase, but will not exceed the initial residual stress maximum in the joint. If the maximum stress peak is exceeded, the dislocation pile-up opening process will be repeated and stress will be relaxed.

In summary, it was shown that by reducing residual stresses in FSW joints with CS will reduce the maximum value of residual stresses and enlarge the area with lower residual stresses, bringing an overall uniform distribution of residual stresses in the joint. With the repeated impact of cold sprayed metal powder particles on the surface of the joint, the maximum value of residual stresses decrease, and the process of dislocation activation→dislocation proliferation→dislocation pile-up→pile-up opening is carried out instead in each grain inside the joint, so that residual stresses in the joint become uniform, dislocation density increases while more uniform.

## 5. Conclusions

In this study, the correlation between microstructure and mechanical properties and residual stress of 2219 aluminum alloy joints prior and after coated with cold spraying was studied. The primary mechanism of stress relief of the joint was identified. The main conclusions are as follow:

- (1) The coating of the 2219 aluminum alloy joint was well bonded to the substrate. The grain size of FSW joint was refined by CS. The plastic deformation of SPE on the surface of the joint during CS increased the geometrically necessary dislocation density of the grains. The proportion of HAGBs and the proportion of recrystallized grains in the joint also increased. The HFE of the CS increased the content of the strengthening phases  $\theta''$  and  $\theta'$  in 2219 aluminum alloy.
- (2) The average hardness of the CS, SPE and HFE joints increased compared to the welded joint. CS played a significant role in improving the tensile strength properties of the joint. The tensile strength was increased from 343 MPa to 398 MPa compared to the welded state, and elongation increased from 4.5% to 10.2%. The SPE was superior to HFE in improving the tensile strength, and HFE was more significant to the improvement of the joint elongation.
- (3) CS significantly reduced residual stresses. The “shot peening effect” of cold spraying was found to be the primary factor to reduce residual stresses, while the “heat flow effect” had negligible effect on stress reduction. In addition, the mechanism of reducing residual stresses was provided by the macroscopic stress-strain theory and the microscopic dislocation theory.

## Declaration of Competing Interest

The authors declare that they have no known competing financial interests or personal relationships that could have appeared to influence the work reported in this paper.

## Data availability

The processed data required to reproduce these findings cannot be shared at this time as the data also forms part of an ongoing study.

## Acknowledgements

The authors would like to acknowledge the financial support from the National Natural Science Foundation of China (No. 52074228, No. 51875470).

## References

- [1] B.X. Xie, L. Huang, Z.Y. Wang, X.X. Li, J.J. Li, Microstructural evolution and mechanical properties of 2219 aluminum alloy from different aging treatments to subsequent electromagnetic forming, Mater. Charact. 181 (2021), 111470.
- [2] D.L. Zlatanovic, S. Balos, J.P. Bergmann, S. Rasche, J. Zavasnik, V. Panchal, L. Sidjanin, S. Goel, In-depth microscopic characterisation of the weld faying interface revealing stress-induced metallurgical transformations during friction stir spot welding, Int. J. Mach. Tools Manuf. 164 (2021), 103716.
- [3] Y.F. Zou, W.Y. Li, Y.X. Xu, X.W. Yang, Q. Chu, Z.K. Shen, Detailed characterizations of microstructure evolution, corrosion behavior and mechanical properties of refill friction stir spot welded 2219 aluminum alloy, Mater. Charact. 183 (2022), 111594.
- [4] R.N. Seerangan, V. Amarnath, A. Rajesh, R. Chinnasamy, V. Balakrishnan, Hardness prediction of post heat treated electron beam welded defense grade AA2219 aluminum alloy for light weight application, Mater. Today: Proc. 68 (5) (2022) 1667–1672.
- [5] Y.H. Zhou, X. Lin, N. Kang, W.D. Huang, Z.N. Wang, Mechanical properties and precipitation behavior of the heat-treated wire + arc additively manufactured 2219 aluminum alloy, Mater. Charact. 171 (2021), 110735.
- [6] Y.T. Lin, M.C. Wang, Y. Zhang, Y.Z. He, D.P. Wang, Investigation of microstructure evolution after post-weld heat treatment and cryogenic fracture toughness of the weld metal of AA2219 VPTIG joints, Mater. Des. 113 (2017) 54–59.
- [7] M.H. Shao, C.M. Wang, H. Zhang, J. Zhang, D.B. Liu, F.F. Wang, Y.J. Ji, G.Q. Chen, Microstructure and corrosion behavior of bobbin tool friction stir welded 2219 aluminum alloy, Mater. Charact. 192 (2022), 112178.
- [8] Y. Su, X.W. Yang, D. Wu, T.X. Meng, W.Y. Li, W.Y. Feng, W.W. Zhao, A. Vairis, Controlling deformation and residual stresses in a TIG joint for invar steel molds, J. Mater. Res. Technol. 27 (2023) 490–507.
- [9] Z.G. Guo, T.J. Ma, X.W. Yang, J. Tao, J. Li, W.Y. Li, A. Vairis, In-situ investigation on dislocation slip concentrated fracture mechanism of linear friction welded dissimilar Ti17( $\alpha+\beta$ )/Ti17( $\beta$ ) titanium alloy joint, Mater. Sci. Eng. A 872 (2023), 144991.
- [10] N.A. Muhammad, P.H. Geng, C.S. Wu, N.S. Ma, Unravelling the ultrasonic effect on residual stress and microstructure in dissimilar ultrasonic-assisted friction stir welding of Al/Mg alloys, Int. J. Mach. Tools Manuf. 186 (2023), 104004.
- [11] S.D. Ji, S.Y. Niu, J.G. Liu, X.C. Meng, Friction stir lap welding of Al to Mg assisted by ultrasound and a Zn interlayer, J. Mater. Process. Technol. 267 (2019) 141–151.
- [12] S.D. Ji, X. Cui, L. Ma, H. Liu, Y.Y. Zuo, Z.Q. Zhang, Achieving high-quality aluminum to copper dissimilar metals joint via friction stir double-riveting welding, Acta Metall. Sin.-Engl. Lett. 36 (4) (2023) 552–572.
- [13] A.S. Sundar, A. Kar, K.K. Mugada, A. Kumar, Enhancement of microstructure, micro-texture, and mechanical properties of Al6061 friction stir welds using the developed static shoulder welding tool, Mater. Charact. 203 (2023), 113148.
- [14] D. Jacquin, G. Guillemot, A review of microstructural changes occurring during FSW in aluminium alloys and their modelling, J. Mater. Process. Technol. 288 (5–8) (2021), 116706.
- [15] Z.G. Guo, T.J. Ma, X. Chen, X.W. Yang, J. Tao, J. Li, W.Y. Li, A. Vairis, Interfacial bonding mechanism of linear friction welded dissimilar Ti2AlNb-Ti60 joint: grain intergrowth induced by combined effects of dynamic recrystallization, phase transformation and elemental diffusion, J. Mater. Res. Technol. 24 (2023) 5660–5668.

- [16] J.V. Christy, A.H.I. Mourad, M.M. Sherif, B. Shivamurthy, Review of recent trends in friction stir welding process of aluminum alloys and aluminum metal matrix composites, *Trans. Nonferrous Metals Soc. China* 31 (11) (2021) 3281–3309.
- [17] Y. Su, X.W. Yang, D. Wu, T.X. Meng, W.Y. Li, W.Y. Feng, A. Vairis, Optimizing welding sequence of TIG cross-joint of invar steel using residual stresses and deformations, *J. Manuf. Process.* 105 (2023) 232–245.
- [18] L. Nie, Y.X. Wu, H. Gong, D. Chen, X.D. Guo, Effect of shot peening on redistribution of residual stress field in friction stir welding of 2219 aluminum alloy, *Materials* 13 (14) (2020) 3169.
- [19] B.H. Huang, L. Wang, X.P. Liu, L. Hui, J.H. Cong, S. Zhou, Effect of ultrasonic impact treatment on corrosion fatigue performance of friction stir welded 2024-T4 aluminum alloy, *Corros. Eng. Sci. Technol.* 57 (3) (2022) 243–253.
- [20] W.T. Hou, M.Z. Oheil, Z.K. Shen, Y.F. Shen, H. Jahed, A. Gerlich, Enhanced strength and ductility in dissimilar friction stir butt welded Al/Cu joints by addition of a cold-spray Ni interlayer, *J. Manuf. Process.* 60 (2020) 573–577.
- [21] A. Fardan, C.C. Berndt, R. Ahmed, Numerical modelling of particle impact and residual stresses in cold sprayed coatings: a review, *Surf. Coat. Technol.* 409 (2021), 126835.
- [22] W.Y. Li, R.R. Jiang, C.J. Huang, Z.H. Zhang, Y. Feng, Effect of cold sprayed Al coating on mechanical property and corrosion behavior of friction stir welded AA2024-T351 joint, *Mater. Des.* 65 (2015) 757–761.
- [23] N. Li, W.Y. Li, X.W. Yang, Y. Feng, A. Vairis, An investigation into the mechanism for enhanced mechanical properties in friction stir welded AA2024-T3 joints coated with cold spraying, *Appl. Surf. Sci.* 439 (2018) 623–631.
- [24] W.Y. Li, N. Li, X.W. Yang, Y. Feng, A. Vairis, Impact of cold spraying on microstructure and mechanical properties of optimized friction stir welded AA2024-T3 joint, *Mater. Sci. Eng. A-Struct. Mater. Prop. Microstruct. Process.* 702 (2017) 73–80.
- [25] W.Y. Li, Y.F. Zou, F.F. Wang, X.W. Yang, Y.X. Xu, K.W. Hu, D.Y. Yan, Employing cold spray to Alter the residual stress distribution of workpieces: a case study on fusion-welded AA2219 joints, *J. Therm. Spray Technol.* 29 (6) (2020) 1538–1549.
- [26] Y.Y. Hu, H.J. Liu, S.S. Du, Achievement of high-strength 2219 aluminum alloy joint in a broad process window by ultrasonic enhanced friction stir welding, *Mater. Sci. Eng. A-Struct. Mater. Prop. Microstruct. Process.* 804 (2021), 140587.
- [27] Q. Wang, X.X. Luo, S. Tsutsumi, T. Sasaki, C.J. Li, N.S. Ma, Measurement and analysis of cold spray residual stress using arbitrary Lagrangian–Eulerian method, *Addit. Manuf.* 35 (2020), 101296.
- [28] Y. Su, W.Y. Li, X.C. Liu, F.Y. Gao, Y. Yu, A. Vairis, Strengthening mechanism of friction stir welded alpha titanium alloy specially designed T-joints, *J. Manuf. Process.* 55 (2020) 1–12.
- [29] P.B. Prangnell, C.P. Heason, Grain structure formation during friction stir welding observed by the 'stop action technique'[J], *Acta Mater.* 53 (11) (2005) 3179–3192.
- [30] M. Calcagnotto, D. Ponge, E. Demir, D. Raabe, Orientation gradients and geometrically necessary dislocations in ultrafine grained dual-phase steels studied by 2D and 3D EBSD, *Mater. Sci. Eng. A-Struct. Mater. Prop. Microstruct. Process.* 527 (10–11) (2010) 2738–2746.
- [31] Y.S. Sato, M. Urata, H. Kokawa, K. Ikeda, Hall-Petch relationship in friction stir welds of equal channel angular-pressed aluminium alloys, *Mater. Sci. Eng. A-Struct. Mater. Prop. Microstruct. Process.* 354 (1–2) (2003) 298–305.
- [32] M. Bhattacharyya, T. Gnaupel-Herold, K.S. Raja, J. Darsell, S. Jana, I. Charit, Evaluation of residual stresses in isothermal friction stir welded 304L stainless steel plates, *Mater. Prop. Microstruct. Process.* 826 (2021), 141982.
- [33] S. Choudhury, T. Medhi, D. Sethi, S. Kumar, B.S. Roy, S.C. Saha, Temperature distribution and residual stress in friction stir welding process, *Mater. Today: Proc.* 26 (2) (2020) 2296–2301.
- [34] Q.N. Meng, M. Wen, C.Q. Hu, S.M. Wang, K. Zhang, J.S. Lian, W.T. Zheng, Influence of the residual stress on the nanoindentation-evaluated hardness for zirconiumnitride films, *Surf. Coat. Technol.* 206 (14) (2012) 3250–3257.
- [35] N. Huber, J. Heerens, On the effect of a general residual stress state on indentation and hardness testing, *Acta Mater.* 56 (20) (2008) 6205–6213.
- [36] L. Wang, H. Bei, Y.F. Gao, Z.P. Lu, T.G. Nieh, Effect of residual stresses on the hardness of bulk metallic glasses, *Acta Mater.* 59 (7) (2011) 2858–2864.
- [37] Y.P. Lu, Mechanism Analysis and Experimental Study on Residual Stress Elimination by Vibration, Zhejiang University, 2002 (In Chinese).